# Quantitative assessment of tomographic proxies for lowermost mantle composition and mineralogy

Justin Leung[a], Andrew M. Walker[a], Paula Koelemeijer[a], Federica Restelli[b], D. Rhodri Davies[c]

[a]*Department of Earth Sciences, University of Oxford, South Parks Road, Oxford OX1 3AN, United Kingdom,*
[b]*Department of Earth Sciences, Queen's Building, Royal Holloway University of London, Egham Hill, Egham, Surrey TW20 0EX, United Kingdom,*
[c]*Research School of Earth Sciences, The Australian National University, Canberra, Australia,*

## Abstract

Large low velocity provinces (LLVPs) dominate Earth's lowermost mantle, but their detailed thermochemical nature remains a topic of discussion. In particular, it is unclear to what extent the bridgmanite to post-perovskite phase transition is able to explain their seismic velocity characteristics. Robust constraints on the origin of these seismic structures would shed light on large-scale mantle dynamics and Earth's thermal and chemical evolution. Here, we examine the combined effects of temperature, chemical heterogeneity and phase transitions on lowermost mantle tomographic signatures. To investigate this, we calculate synthetic seismic velocities expected from a range of scenarios for the stability of post-perovskite combined with models of different lowermost mantle temperatures and compositions using recent thermodynamic data. These are filtered to account for limited tomographic resolution, allowing for quantitative comparisons between our synthetic seismic velocities and a recent Backus-Gilbert based tomography model. Cru-

cially, this model provides robust ratios and correlations of velocity anomalies derived from nearly identical $V_p$ and $V_s$ resolution, and includes uncertainty quantification that accounts for both data and theoretical errors. Given the tomographic uncertainties and limited resolution, our comparisons focus on globally and depth averaged seismic characteristics, which capture the effects of lateral compositional and mineralogical variability. By rejecting synthetic models that do not fit within tomographic uncertainties, we quantitatively eliminate the following: (i) models containing LLVPs with an iron-rich primordial composition, as these generate anomalously high root mean square seismic velocity anomalies; and (ii) models without post-perovskite in the lowermost mantle, as these cannot explain observations of elevated ratios of shear-wave to compressional-wave velocity ($R_{s/p}$) and a negative correlation between variations in shear-wave and bulk sound velocity ($r_{s-c}$). Additionally, we demonstrate that observations of $R_{s/p}$ and $r_{s-c}$ in the lowermost mantle cannot be explained by thermochemical LLVPs alone, but require bridgmanite and post-perovskite to co-occur at depth in the mantle. As such, we demonstrate that globally averaged seismic velocity characteristics can distinguish between composition and mineralogy in the lowermost mantle.

*Keywords:* LLVPs, Post-perovskite, SOLA, Lowermost mantle composition, Uncertainties, Seismic tomography

---

## 1. Introduction

Large low velocity provinces (LLVPs) are two seismically slower structures lying in the lowermost mantle beneath the Pacific and Africa, spanning 25 % of the core-mantle boundary (CMB) with estimated negative S-wave velocity anomalies of 1.5-5% (Cottaar and Lekic, 2016; McNamara, 2019). Because of their size, LLVPs have large influences on planetary scale dynamics, such as the influence of density variations on the global mantle flow, which also results in dynamic topography of the surface and CMB (Hager et al., 1985; Garnero et al., 2016; Richards et al., 2023; Davies et al., 2023). Therefore, understanding the origin and thermochemical structure of these deep mantle features provides a way to better interpretation of the coupling between the outer core and the mantle, which links to heat flux from the core (McNamara, 2019; Schuberth et al., 2009a), geomagnetic reversals (Tarduno et al., 2015), and the generation and stability of mantle plumes (Burke et al., 2008; Tarduno et al., 2015; Thorne et al., 2004). However, determining the composition of LLVPs is difficult because of the non-unique relationship of seismic wave speeds to pressure, temperature, composition and mineral phases. Hence, the origin of LLVPs remains contested, particularly focusing on the extent to which they are thermochemical.

Lowermost mantle tomographic signatures include an anti-correlation between shear-wave velocity anomalies ($d\ln V_s$) and bulk sound velocity anomalies ($d\ln V_c$) (hereafter referred to as $r_{s-c}$) and the elevated ratio of shear-wave to compressional-wave velocity anomalies ($R_{s/p} = d\ln V_s / d\ln V_p$) between 2.6 and 3.4 (Masters et al., 2000; Moulik and Ekström, 2016; Ritsema and Van Heijst, 2002; Su and Dziewonski, 1997). However, seismic signatures gen-

erated by pure thermal variations (in the absence of temperature-dependent phase transitions) only show strongly positive values of $r_{s-c}$ and $R_{s/p}$ below 2.5 because both the bulk and shear moduli soften with increasing temperature, in the absence of temperature-dependent phase transitions (Karato and Karki, 2001). This means that observations of $r_{s-c}$ and $R_{s/p}$ cannot be explained by thermal effects alone, which therefore have been interpreted as evidence for LLVPs of thermochemical origin. This interpretation has been supported by other geophysical and geochemical observations, including the correlation of LLVP edges with hotspots containing enriched isotope signatures (Burke et al., 2008; Thorne et al., 2004), steep $V_s$ gradients of 1.3—6 %/100 km (Ni et al., 2002), and the anti-correlation between $V_s$ and density inside (and outside) LLVPs (Ishii and Tromp, 1999; Trampert et al., 2004). However, other studies have suggested that temperature variations alone can explain velocity gradients at LLVP margins, particularly: (i) in geodynamic models with a substantial CMB heat flux as expected from current constraints; and (ii) when anelastic effects on seismic velocity are considered (e.g. Schuberth et al., 2009b; Davies et al., 2012). Furthermore, recent observations imply lower $V_s$ gradients at the edges of LLVPs (Ward et al., 2020). Additionally, our ability to resolve lowermost mantle density from seismic and geodetic data remains debated, due to limited data and the trade-off of density with $V_p$, $V_s$ in seismic data (Akbarashrafi et al., 2018; Robson et al., 2021) and viscosity in geodetic observables (Forte et al., 2015).

Even if LLVPs are thermochemical, multiple compositions can explain the characteristics of observed anomalies. One possible composition is the preservation of primordial mantle material segregated during top-down crys-

tallisation of a basal magma ocean (BMO, Labrosse et al., 2007), which is enriched with iron-rich melts generated in the primordial mantle transition zone (Lee et al., 2010). A second proposed composition is that LLVPs are made of subducted iron- and silicon-rich Hadean crust along with a terrestrial regolith comprising chondritic and solar-wind-implanted material (Tolstikhin and Hofmann, 2005). These two scenarios suggest that LLVPs are formed of primordial material, and thus imply that they are long-lived structures throughout Earth's evolution. Alternatively, LLVPs could be piles of accumulated recycled oceanic crust from subducted slabs (Niu, 2018), which are denser than the background mantle at lowermost mantle pressures (Hirose et al., 2005). This would imply that LLVPs are metastable features with material constantly being added and removed, and therefore would have less well defined margins (Jones et al., 2020; Panton et al., 2025).

Yet, numerous studies (e.g. Davies et al., 2012; Schuberth et al., 2009b) have suggested that elevated ratios and anti-correlations in the lowermost mantle do not require compositional heterogeneity. They favour an alternative explanation due to the bridgmanite-post-perovskite (bdg-pPv) phase transition, which experimental results indicate to happen at 200-300 km above the CMB (Murakami et al., 2004; Oganov and Ono, 2004). The phase transition exhibits a 1-4% increase in $V_s$, a small change in $V_p$ and a decrease in $V_c$, which results in a higher $R_{s/p}$ and a negative $r_{s-c}$ (Cobden et al., 2015; Oganov and Ono, 2004; Tsuchiya et al., 2004). The large Clapeyron slope of the bdg-pPv phase transition, the proposed 3-4 order-of-magnitude decrease in viscosity and the increase in thermal diffusivity of post-perovskite relative to bridgmanite is thought to destabilise the thermal boundary layer

above the CMB and promote plume formation (Ammann et al., 2010; Hirose, 2006; Hunt et al., 2012). LLVPs of thermal origin have been suggested as plumes focused into clusters by adjacent regions dominated by subduction (Bull et al., 2009; Davies et al., 2012; Schubert et al., 2004). Nonetheless, large uncertainties in mineral physics at lowermost mantle temperature and pressure conditions indicate that the phase transition is still poorly understood (Cobden et al., 2015). Additionally, the composition of bridgmanite and post-perovskite, poorly constrained in the lowermost mantle, affects both the phase transition pressure (hence depth) and two-phase region. In particular, the incorporation of iron increases the thickness of the two-phase region and decreases the pressure at which the phase boundary occurs (Catalli et al., 2009).

Previous studies (e.g. Davies et al., 2012; Koelemeijer et al., 2018) have conducted synthetic-tomographic comparisons to determine whether compositional heterogeneity (chemical) or phase transitions (mineralogical) better explain lowermost mantle seismic signatures. However, Davies et al. (2012) only investigated models which included the presence of post-perovskite, and therefore were limited by scenarios where both chemical and mineralogical effects are important. Koelemeijer et al. (2018) investigated both, but different post-perovskite scenarios were artificially created, and only pyrolite and basaltic LLVP compositions were considered. Additionally, the tomography models used in these studies only had similar, but not identical resolution for $d\ln V_s$ and $d\ln V_p$, which is important for obtaining robust velocity ratios and correlations. In this study, we therefore examine the combined effects of LLVP composition and the bdg-pPv phase transition on lowermost mantle

seismic velocity anomalies, ratios and correlations. We expand on the study of Koelemeijer et al. (2018) by examining different LLVP compositions, utilising up-to-date and self-consistent thermodynamic parameters, and using a tomographic model with nearly equal resolution on $d\ln V_s$ and $d\ln V_p$ that includes uncertainty quantification. This enables us to quantitatively assess models of LLVP compositions and post-perovskite stability scenarios by eliminating synthetic seismic velocity models that fall outside of tomographic uncertainties.

## 2. Methods

To address the relative effects of composition and mineralogy on seismic signatures in the lowermost mantle, we compare observations from seismic tomography (Restelli et al., 2024) with synthetic seismic velocity models of various LLVP composition and post-perovskite stability scenarios (Fig. 1). To generate these synthetic models, we utilise realistic temperature and compositional fields from previous geodynamic modelling (Davies et al., 2012, section 2.1). We calculate the equilibrium phase assemblages for a range of LLVP compositions and post-perovskite stability scenarios (section 2.2). By combining the temperature field and equilibrium phase assemblages, we calculate synthetic seismic velocity models, which are filtered to account for the limited resolution of the observation-based seismic tomography model (section 2.3). Only after filtering can we quantitatively compare the predicted seismic velocity models with tomographic observations, where we reject synthetic seismic velocity models that fall outside of the available tomographic uncertainties (section 2.4).

### *2.1. Geodynamic model*

We use high-resolution global mantle circulation models from Davies et al. (2012), which were originally designed to investigate the origin of LLVPs. These models were based on a modified version of TERRA (Davies et al., 2013), a finite-element mantle convection code that solves the conservation equations of mass, momentum and energy at infinite Prandtl number (Stokes flow) in a spherical shell. A mesh of 80 million grid points (∼25 km grid cells) enabled simulations at an Earth-like Rayleigh Number ($Ra \approx 5 \times 10^8$).

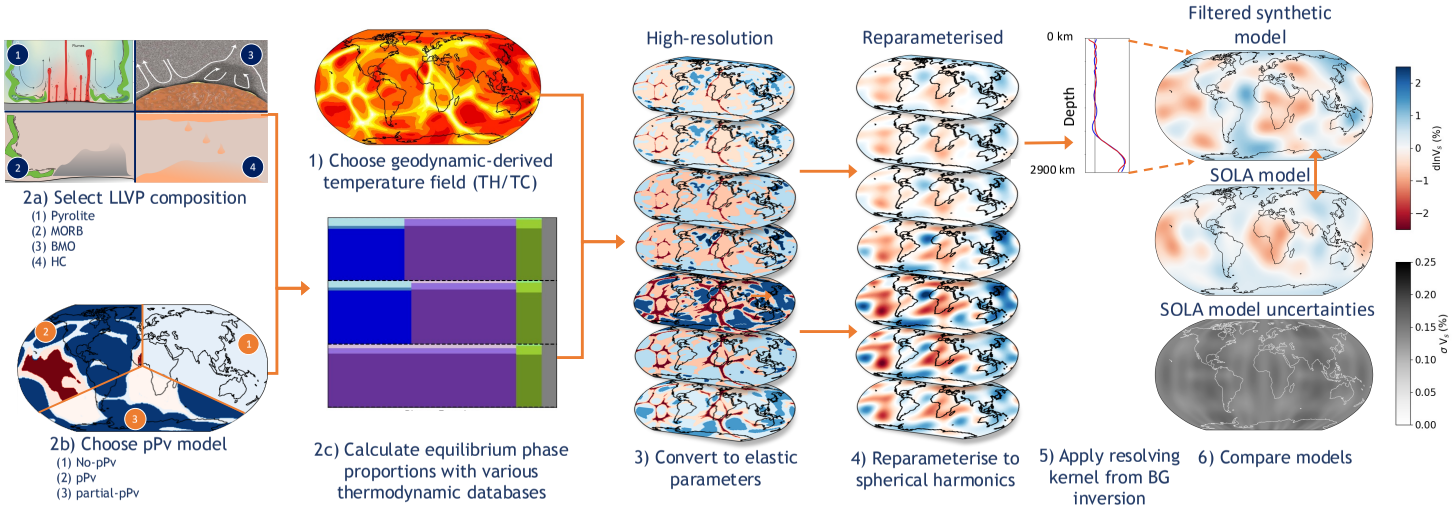


Figure 1: A schematic of the workflow to generate and compare synthetic seismic velocity models with tomographic results. Each step is expanded on in the text. MORB = Mid-ocean ridge basalt, BMO = Basal magma ocean, HC = Hadean (early Earth) crust, pPv = post-perovskite, SOLA Model = Subtractive Optimally Localised Averages tomographic model, referring to the model from Restelli et al. (2024).

Simulations incorporated compressibility, in the form of the anelastic liquid approximation. The viscosity was temperature- and depth-dependent, with jumps below the lithosphere and at the 410- and 660-km phase transitions. Dynamic effects of the post-perovskite phase transition were not considered. These models were bounded by isothermal boundary conditions of 300 K at the surface and 4000 K at the CMB. A free-slip boundary condition was imposed at the CMB, while surface motion was governed by a plate model with 300 Myr of plate motion history (Stampfli and Borel, 2002; Stampfli and Hochard, 2009). The imposed plate motion captured the effects of surface-plate strength and plate-boundary weakness on convection, and improved spatio-temporal constraints on long-wavelength mantle structures, allowing for predictions of the mantle's thermal structure in space and time. Thermochemical models included a compositional field ($X$) simulated by the ratio tracer particle method, with $\approx 2.0 \times 10^9$ active tracers of two distinct types (dense material, $X = 1$; regular material, $X = 0$). Altogether, the simulation of Earth-like mantle convection, multi-parameter dependent viscosity profiles, boundary conditions governed by 300 Myr of plate motion, and particle tracing of compositional heterogeneity enabled this suite of models to generate synthetic mantle structures with a comparable distribution of heterogeneity as observed seismically. This is evidenced by their successful comparison against numerous seismic tomographic models (e.g. S40RTS, Ritsema et al. 2011; SP12RTS, Koelemeijer et al. 2016) and other seismological observations, via several tomographic-geodynamic comparison studies (e.g. Davies et al., 2015; Koelemeijer et al., 2018; Trautner et al., 2023).

We utilise the temperature and compositional outputs of the geodynamic

models as inputs for our synthetic seismic velocity model calculations. We use two temperature fields from Davies et al. (2012): (i) a purely thermal (TH) model without any chemical heterogeneity; and (ii) a thermochemical (TC) model, with chemically distinct, denser material (2.75 % higher intrinsic density) resembling large-scale piles in the lowermost mantle. Similar to Davies et al. (2012) and Koelemeijer et al. (2018), the availability of different temperature fields for a thermal and thermochemical mantle enables us to compare our suite of LLVP composition models in a self-consistent manner. The compositional field represents the fraction of chemically distinct material within a grid cell. In our thermochemical models, we define LLVPs to be at locations where $X \geq 0.6$. We find that the choice of this compositional threshold has no major effect on the spatial definition of LLVPs as changes in $X$ from 0 to 1 occur over short distances, due to the fact that chemical diffusivity is negligible.

### *2.2. Calculating equilibrium phase assemblages*

To calculate the equilibrium phase assemblages for our synthetic models, we utilise a constrained free energy minimisation algorithm in BurnMan (Myhill et al., 2023). Rather than solving the full Gibbs Energy minimalisation problem for all known phases, this solver optimises equilibrium relations (phase proportions and compositions) for fixed assemblages (phases that are present). The fixed assemblages are pre-determined from known major phase assemblages for the various LLVP compositions (Irifune and Tsuchiya, 2015; Stixrude and Lithgow-Bertelloni, 2011, 2021). Because the major mineral phases in the lowermost mantle are relatively well-known and thought to remain relatively constant throughout lowermost mantle pressures

and temperatures for a given composition, the BurnMan solver outputs identical results to a full Gibbs Energy minimiser (e.g. HeFESTo, Stixrude and Lithgow-Bertelloni, 2021). Thus, by avoiding the full Gibbs Energy minimisation, the BurnMan solver calculates equilibrium phase assemblages with a substantially lower computational cost. For the calculation, we utilise up-to-date thermodynamic parameters from the SLB2022 (Stixrude and Lithgow-Bertelloni, 2021) mineralogical model, which includes improved calculations for the pressure dependence of non-ideal solution parameters such as the bulk modulus. To perform this energy minimisation calculation, four pieces of information are needed: (i) temperature; (ii) pressure (depth); (iii) oxide composition, here represented with 6 components; and (iv) the assemblage, including any constraints on the stability of bridgmanite, post-perovskite and the co-existence of both phases. The fixed mineral assemblage as input for the energy minimisation is determined by the post-perovskite stability and 6-oxide-component composition (detailed in Table S1). The temperature field is obtained from the geodynamic model (see above), and the pressure field is obtained by converting the depth in the geodynamic model of Davies et al. (2012) using PREM (Dziewonski and Anderson, 1981). Unfortunately, the full covariance matrix for the equation of state parameters is unavailable for this database. Consequently, as elaborated on in the discussion, we cannot include uncertainties on the thermodynamic parameters in our calculations.

We fix the ambient mantle to have a pyrolite composition, only varying the composition of the LLVPs between the different synthetic seismic velocity models. We examine four different LLVP compositions (Table S1), each representing a proposed origin (see the Introduction). We first consider LLVPs

as purely thermal features, where LLVPs have a pyrolite composition. To be self-consistent with the geodynamic simulation, we use the TH temperature field for this LLVP composition (black line in Fig. 2a). We use the TC temperature field (black line in Fig. 2b-d) for the other three LLVP compositions: recycled oceanic crust (MORB), remnants of basal magma ocean (BMO), and Hadean crust (HC). We therefore extend the study of Koelemeijer et al. (2018), who only considered a basaltic (MORB) thermochemical composition. For each LLVP composition, we specify a mineral assemblage using the SLB2022 mineralogical database (Stixrude and Lithgow-Bertelloni, 2021) as input for the energy minimisation (see supplementary material).

The ambiguity in the stability of bridgmanite and post-perovskite is due to large uncertainties in thermodynamic parameters of the bridgmanite-post-perovskite (bdg-pPv) phase boundary. To address this ambiguity, we implement three different post-perovskite stability scenarios per LLVP composition. The first scenario inhibits any existence of post-perovskite in the lowermost mantle, representing a phase boundary that occurs at temperatures and pressures higher than the CMB (hereafter termed the "no-pPv" scenario), and allowing us to isolate the effects of post-perovskite from LLVP composition. The second scenario allows post-perovskite to be stable in the lowermost mantle (hereafter termed the "pPv" scenario) at P-T conditions determined by the thermodynamic mineralogical model (Fig. 2). The third scenario is a mixture of the first two, with post-perovskite restricted to occur solely outside of LLVPs, i.e. at low temperature (hereafter termed the "partial-pPv" scenario). We include this scenario because the post-perovskite phase transition has a positive Claperyon slope, making it

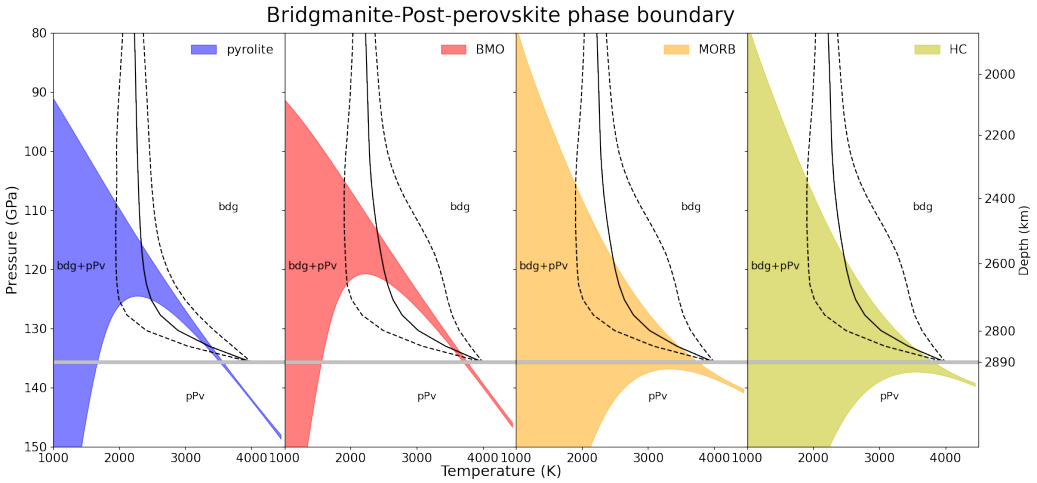


Figure 2: The bridgmanite post-perovskite phase transition calculated using the SLB2022 mineralogical model for the four considered LLVP compositions: (a) pyrolite, (b) BMO (Basal magma ocean), (c) MORB (Mid-ocean ridge basalt), (d) HC (Hadean (early Earth) crust). The shaded area in each plot represents the two-phase region, which indicates the pressure and temperature conditions where both bridgmanite and post-perovskite occur. The solid and two dashed black lines show the mean, 10, and 90 percentile temperature, respectively, at each depth of the (a) TH and (b,c,d) TC temperature fields from Davies et al. (2012). The horizontal silver line indicates the pressure at the CMB. The wedge-like stability of the two-phase region is specific to this mineralogical model, where bridgmanite remains stable at high pressures and low temperatures due to strong partitioning of aluminium into bridgmanite at these conditions.

less likely for post-perovskite to occur in LLVPs as they are thought to be warmer than the surrounding mantle. This is supported by observations of post-perovskite detected mostly in the colder regions of the lowermost mantle (Cobden et al., 2015). We implement these three post-perovskite scenarios with a thermodynamically self-consistent approach by directly including or omitting the post-perovskite phase in the fixed assemblage before optimis-

ing for equilibrium phase proportions in BurnMan. This is an improvement compared to Koelemeijer et al. (2018), who artificially shifted the bdg-pPv phase boundary to consider different post-perovskite stability scenarios.

### *2.3. Tomographic observations*

We compare our synthetic seismic velocity models with tomographic observations from Restelli et al. (2024), derived using the Subtractive Optimally Localised Averages (SOLA) method. The SOLA method is a variant of Backus-Gilbert theory that calculates some optimally-localised average ($\hat{m}$) over the "true" model $m^t$ (Zaroli, 2016). The averaging process removes the non-uniqueness in the solution, such that additional regularisation terms (e.g. model smoothness) are not needed to constrain the solution. The average can be expressed as

$$\hat{m} = \int \hat{R} m^t + (\text{propagated noise}), \tag{1}$$

where $\hat{R}$ is the resolving kernel that is optimised to match a pre-defined target kernel (Restelli et al., 2024; Zaroli, 2016). The advantage of optimising for a resolving kernel is to provide direct control of the local model resolution, which here provides equal resolution on both $d\ln V_p$ and $d\ln V_s$. Therefore, we can calculate robust values of ratios and correlations between $d\ln V_s$ and $d\ln V_p$, and consequently also $d\ln V_c$, given that the SOLA-derived averages refer to the same region inside the Earth. Other tomographic models can only ensure similar but not equal resolution for $d\ln V_s$ and $d\ln V_p$, such that ratios and correlations of velocity anomalies may include inversion artefacts (e.g. Koelemeijer et al., 2018). Another benefit of this method is the availability of a quantified tomographic uncertainty that trades off with resolution. This

uncertainty can be used as a concrete constraint, allowing us to quantitatively rule out synthetic seismic velocity models that fall outside the uncertainty range. This provides a rigorous method to compare geodynamic and tomographic models, in contrast to previous studies (e.g. Koelemeijer et al., 2018; Schuberth et al., 2009b) that were only able to assess the relative fit of their synthetic models. Recently, Su et al. (2023) utilised an alternative approach to address the difference in resolution, cross-filtering $d\ln V_s$ and $d\ln V_p$ models to obtain similar resolution between the two and to calculate ratios of velocity anomalies. However, this approach does not provide the required uncertainty information for quantitative comparisons.

The tomographic results of Restelli et al. (2024) were obtained from the splitting functions of 143 spheroidal normal modes that are sensitive to the crust and the mantle. The model was laterally parameterised in spherical harmonics of even degrees up to degree 8, such that 1-D inferences with uncertainty bounds could be conducted independently for each spherical harmonic coefficient. The uncertainties encompassed both data and theoretical errors, with a factor of 2 applied to the data uncertainties to account for theoretical errors due to the use of the self-coupling approximation (Akbarashrafi et al., 2018; Robson et al., 2021). Additionally, Restelli et al. (2024) included the simultaneous sensitivity of normal modes to multiple physical parameters (e.g. $V_p$ and $\rho$) as additional 3-D noise (Masters and Gubbins, 2003), such that the effects of unmodelled parameters are captured in the uncertainties. The final model consists of four layers of averaged velocities, with the lowest layer having sensitivity to the lowermost mantle between depths of 2100 km and 2890 km (CMB). We use the $V_p$ and $V_s$ from this layer to compare with

287 our synthetic seismic velocity models (Fig. 3).

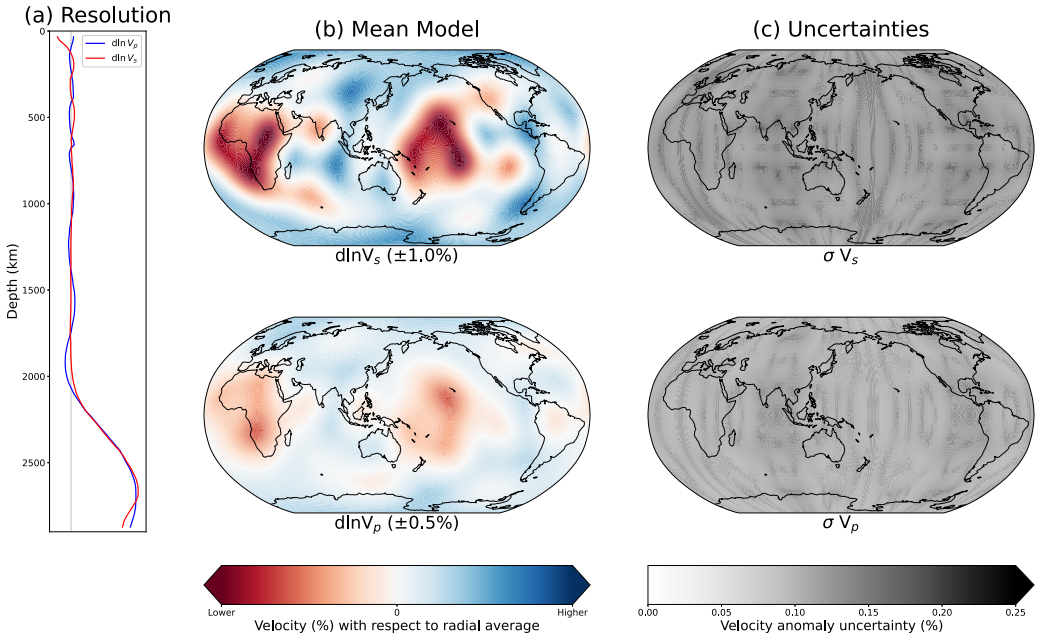


Figure 3: A plot summarising the tomographic model of Restelli et al. (2024) in the deep mantle. a) The resolving kernels for $d\ln V_p$ (blue) and $d\ln V_s$ (red) are nearly identical and therefore indicate an almost equal $V_s$ and $V_p$ resolution. Mean amplitudes (b) and uncertainties (c, $1\sigma$) are shown for $d\ln V_s$ (top) and $d\ln V_p$ (bottom). The maximum of the scale for $d\ln V_s$ ($\pm 1.0\%$) is twice that of $d\ln V_p$ ($\pm 0.5\%$), so that the two plots have similar colour intensity and patterns for $R_{s/p} = 2$.

288 To quantitatively compare our synthetic seismic velocity models with the
289 tomography model, we apply the resolving kernel to our synthetic models.
290 The resolving kernel accounts for the difference in resolution between the
291 geodynamic model (e.g. ∼25 km) and the tomographic model (e.g. ∼5000
292 km wavelength for spherical harmonic degree 8), thus it is synonymous with
293 the tomographic resolution operator available for other tomographic mod-
294 els (e.g. S40RTS, Ritsema et al. 2011; SP12RTS, Koelemeijer et al. 2016).

The resolving kernel condenses the synthetic seismic velocity models into a weighted depth average that can be directly and quantitatively compared with the tomographic observations.

### *2.4. Calculation of quantitative metrics*

The synthetic seismic velocities (calculated on a real-space grid) are first parameterised in the same spherical harmonic basis as used for the observed tomography (Edmonds, 1960). To evaluate their amplitudes, we compute the root mean square (RMS) of shear-wave velocity anomalies ($d\ln V_s$) and compressional-wave velocity anomalies ($d\ln V_p$) as:

$$d\ln V_s = \sqrt{\frac{\sum_{l=0}^{8}\sum_{m=-l}^{l} f_{lm}^2}{4\pi}}, \tag{2}$$

$$d\ln V_p = \sqrt{\frac{\sum_{l=0}^{8}\sum_{m=-l}^{l} g_{lm}^2}{4\pi}}, \tag{3}$$

with $f_{lm}$ and $g_{lm}$ representing the spherical harmonic coefficients for $d\ln V_s$ and $d\ln V_p$ respectively at degree $l$ and order $m$. Similar to Koelemeijer et al. (2018), the $d\ln V_s/d\ln V_p$ ratio ($R_{s/p}$) is taken by dividing the RMS values of $d\ln V_s$ and $d\ln V_p$:

$$R_{s/p} = \sqrt{\frac{\sum_{l=0}^{8}\sum_{m=-l}^{l} f_{lm}^2}{\sum_{l=0}^{8}\sum_{m=-l}^{l} g_{lm}^2}}. \tag{4}$$

We calculate tomographically filtered predictions of $d\ln V_c$ by applying the respective resolving kernels separately to the synthetic $d\ln V_s$ and $d\ln V_p$ models to obtain filtered $d\ln V_s$ and $d\ln V_p$ models, and then combining these using (see eq.2 in Masters et al. (2000)):

$$d\ln V_c(z) = \frac{d\ln V_p(z) - \gamma(z) d\ln V_s(z)}{1-\gamma(z)} \tag{5}$$

where $\gamma(z) = \frac{4}{3}\frac{V_s^2(z)}{V_p^2(z)}$, and $V_s$ and $V_p$ are the radially averaged absolute shear-wave and compressional-wave velocities at depth $z$. The $d\ln V_s$-$d\ln V_c$ correlation ($r_{s-c}$) is then calculated by:

$$r_{s-c} = \frac{\sum_{l=0}^{8}\sum_{m=-l}^{l} f_{lm}h_{lm}}{\sqrt{\sum_{l=0}^{8}\sum_{m=-l}^{l} f_{lm}^2 \sum_{l=0}^{8}\sum_{m=-l}^{l} h_{lm}^2}}, \tag{6}$$

with $h_{lm}$ representing the spherical harmonic coefficients for $d\ln V_c$ at degree $l$ and order $m$.

To obtain uncertainties for the RMS $d\ln V_s$, RMS $d\ln V_p$, $R_{s/p}$ and $r_{s-c}$, we treat each of the spherical harmonic coefficients as Gaussian variables (with the associated uncertainty as the standard deviation) and conduct 1,000,000 realisations (drawing each time a sample for each coefficient in the sum) to obtain distributions for each of the seismic characteristics listed above. For each of the four distributions, we then obtain the median, $1\sigma$ (68%) uncertainty range and $2\sigma$ (95.4%) uncertainty range. We subsequently reject synthetic models that do not fit within the $2\sigma$ uncertainty range of either both observed RMS velocities, or both the observed $R_{s/p}$ and $r_{s-c}$.

## 3. Results

### *3.1. Amplitudes of velocity anomalies*

All of the synthetic seismic velocity models generate degree-2 structures that resemble tomographic observations: the two LLVPs beneath Africa and the Pacific, surrounded by fast anomalies (Fig 4 and S1). The Pacific slow anomaly appears to be shifted eastward compared to its location in the tomography model of Restelli et al. (2024), which is likely due to uncertainties around the plate reconstructions and reference frame. Within the LLVPs, the $d\ln V_s$ amplitudes of the synthetic seismic velocity models fall within the range of 1.5-5% (the range of seismic tomography models summarised by McNamara (2019)). However, the amplitudes are considerably higher in iron-rich LLVP compositions (BMO and HC) compared to the tomographic model of Restelli et al. (2024), as suggested in previous studies (e.g. Davies et al., 2012). This is because the higher iron content and temperature both decrease $V_s$ to generate larger velocity variations.

To quantitatively assess the amplitudes, we compare the RMS velocities of the different filtered synthetic seismic velocity models with tomographic observations (Fig. 5). We see that the amplitudes of velocity anomalies are more affected by LLVP composition than the presence of post-perovskite. Here, we note that, apart from the effects of composition itself, synthetic models for different LLVP compositions also encapsulate the effects of temperature on seismic observables because of the different temperature fields used for thermal and thermochemical LLVP scenarios. The RMS for $d\ln V_s$ (Fig. 5b) in models without post-perovskite and with post-perovskite of the same composition (same colour, different symbols) differ by no more than 0.4

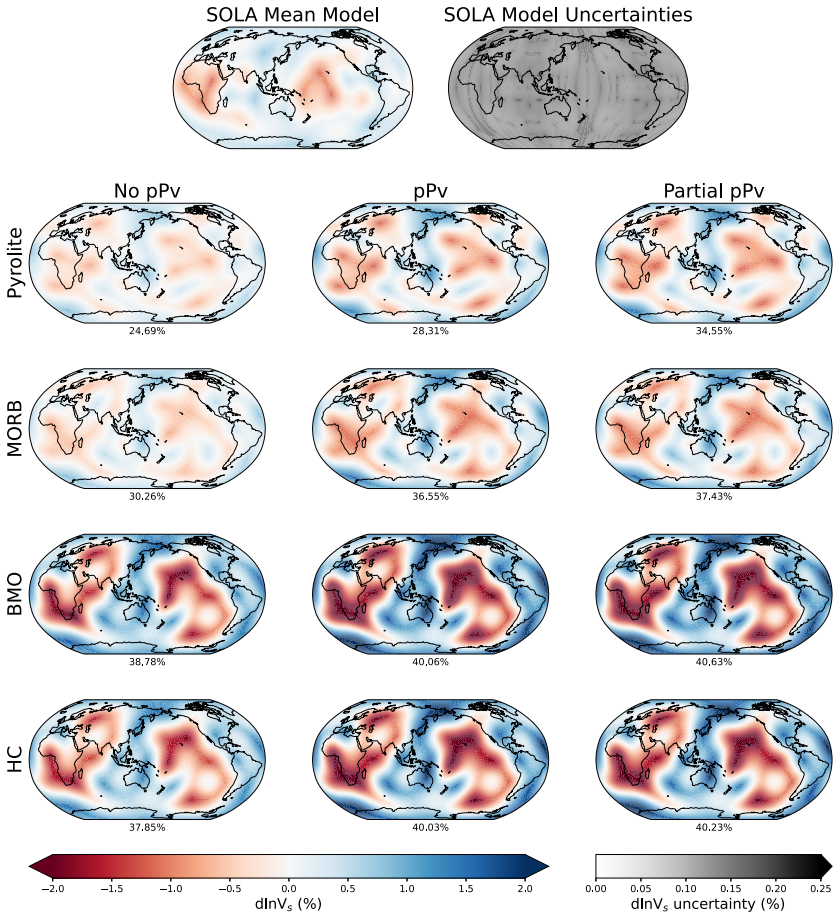


Figure 4: Depth slices for $d \ln V_s$ amplitudes of the filtered synthetic seismic velocity models, organised by post-perovskite (pPv) scenario in columns and LLVP composition in rows. The mean and uncertainty ($1\sigma$) of the tomography model of Restelli et al. (2024) in the lowermost mantle are shown on the top. Acronyms for the compositions (row labels) are the same as those in Fig. 2. The percentage below each plot is the areal coverage of the LLVPs, which is calculated by finding the areal extent where $d \ln V_s \leq -0.3\%$ (similar as in other studies, e.g. Koelemeijer et al., 2017; Lau et al., 2017)

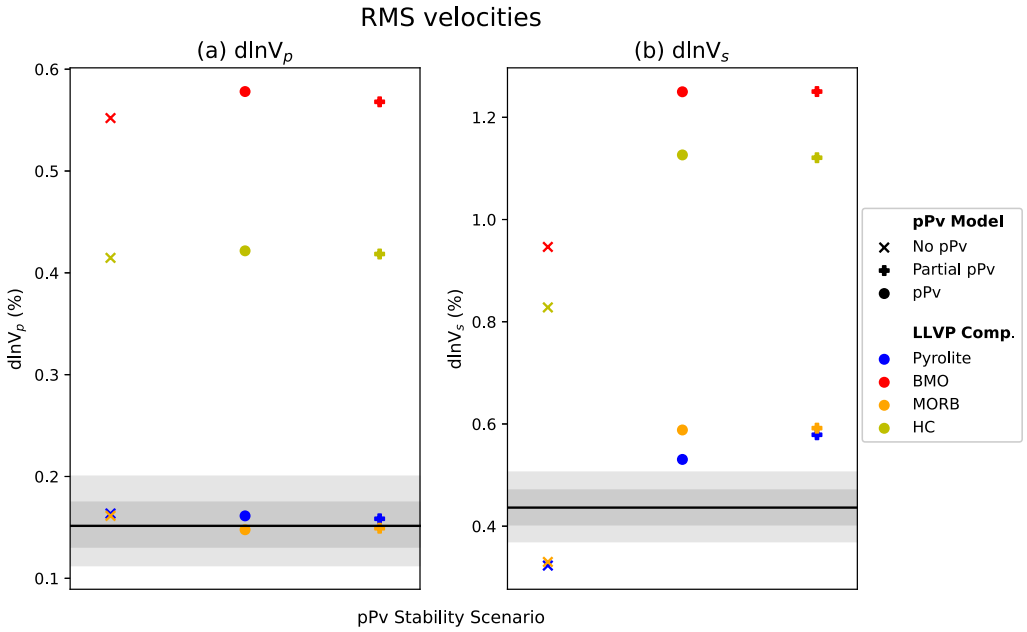


Figure 5: Root mean square of (a) $d\ln V_p$ and (b) $d\ln V_s$ from filtered synthetic seismic velocity models. The colour and symbol of each point represent the LLVP composition and post-perovskite scenario of the synthetic model, respectively (see the figure legend for more details). Black lines and grey shaded regions show the mean and uncertainty of the tomography model of Restelli et al. (2024) respectively, where the darker and lighter shading refers to the region of $1\sigma$ and $2\sigma$ respectively.

352 %, whereas the velocity amplitudes can differ up to 0.8 % between models of
353 different LLVP compositions (same symbol, different colours). The RMS val-
354 ues for $d\ln V_p$ are indistinguishable across models of different post-perovskite
355 scenarios for the same LLVP composition (Fig. 5a). Both pyrolite (blue)
356 and MORB (orange) LLVP compositions fit within $1\sigma$ of tomographic ob-
357 servations, whereas iron-rich compositions (BMO, red and HC, khaki) have
358 RMS values for $d\ln V_p$ that are at least three times larger than the observed
359 tomographic value. However, none of the models fit the RMS of $d\ln V_s$ within

the $2\sigma$ uncertainty region of the tomographic observations of Restelli et al. (2024). Nonetheless, models with pyrolite or MORB LLVP compositions have RMS values that are closer to tomographic observations than the iron-rich LLVP compositions. Note that these are either too low or too high depending on whether post-perovskite is excluded or included, respectively. This indicates that it is possible to fit both $d\ln V_s$ and $d\ln V_p$ by changing the post-perovskite model. In contrast, synthetic models with iron-rich LLVP compositions have RMS values for $d\ln V_s$ that are at least twice as large as the mean value of the tomographic model. Therefore, based on the seismic velocity amplitudes, it is unlikely that the LLVPs are entirely made up of material with a high iron composition. This is in agreement with the considerably high LLVP coverage (Fig. 4) of these iron-rich models in relation to the 25% coverage observed on the CMB (Cottaar and Lekic, 2016).

### *3.2. Ratios and correlations of velocity anomalies*

To better understand the behaviour of the ratios and correlations of velocity variations with depth in the lowermost mantle, we first consider their values in the synthetic seismic velocity models before filtering (Fig. 6), where depth information has not yet been removed by the filtering process (step 4-6 in Fig 1). In Fig. 6, we find similar shapes across all compositions: "n-shaped arches" in $R_{s/p}$ (top row) and "u-shaped arches" in $r_{s-c}$ (bottom row). $R_{s/p}$ increases sharply between post-perovskite fractions of 0 to around 0.2, then increases very gradually and reaches a peak value between post-perovskite fractions of 0.2 and 0.8, before it decreases sharply back to 2 above a post-perovskite fraction of 0.8. Similar to $R_{s/p}$, there are sharp changes in $r_{s-c}$ at post-perovskite fractions below 0.2 and above 0.8, reaching maximum nega-

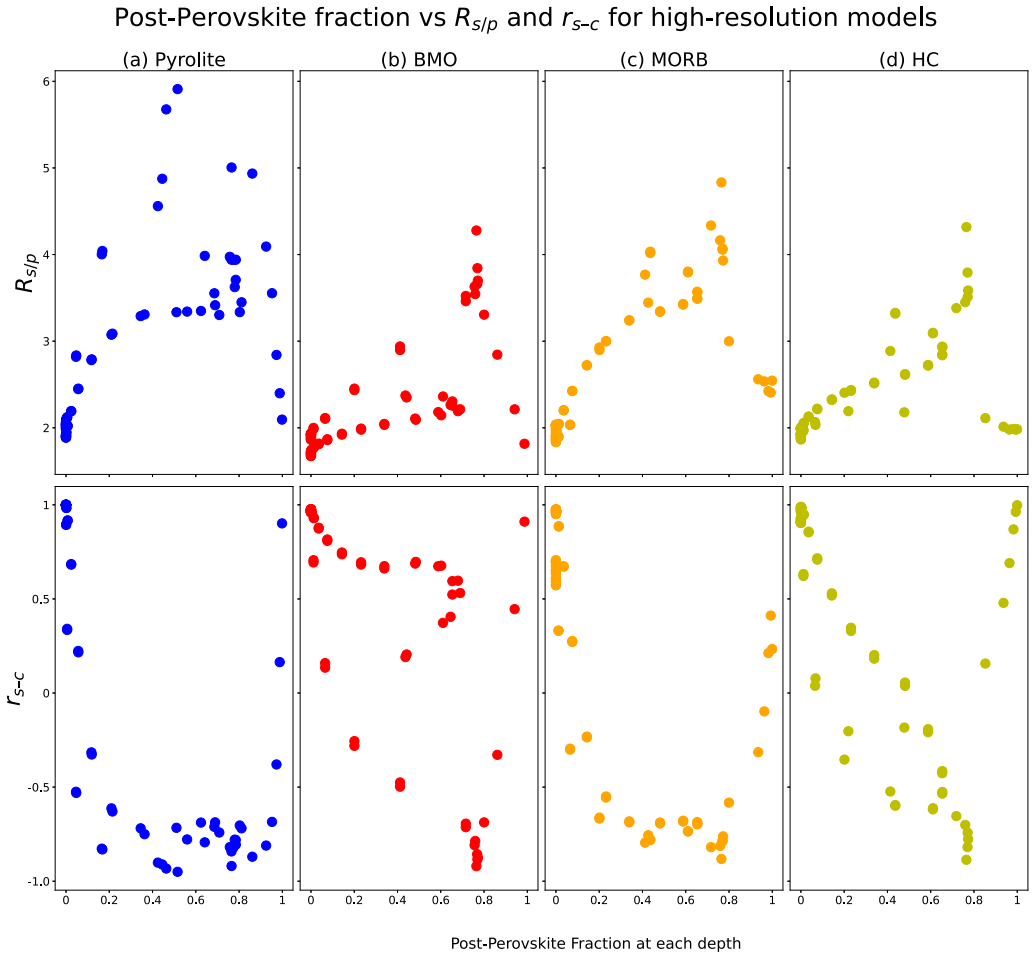


Figure 6: $R_{s/p}$ ($d\ln V_s/d\ln V_p$, top) and $r_{s-c}$ ($d\ln V_s - d\ln V_c$ correlation, bottom) at each depth in synthetic seismic velocity models before filtering, plotted against the average post-perovskite fraction at each depth. Each circle represents an averaged post-perovskite fraction value over a depth layer in the unfiltered models, such that a point with a post-perovskite fraction equal to 0 represents a depth layer with no post-perovskite, and 1 represents a depth layer with no bridgmanite. Each column of subplots corresponds to the LLVP composition used for the specific suite of synthetic seismic velocity models, which is colour-coded the same as in other plots in the paper for consistency. See Fig. 2 for LLVP composition acronyms.

tive correlation values at intermediate post-perovskite fractions. The main differences in $R_{s/p}$ and $r_{s-c}$ between LLVP compositions are their respective peak values are the steepness of the "arches". Models with pyrolite (Fig 6a) and MORB (Fig 6c) LLVP compositions show relatively symmetric "arches", reaching peak values of $R_{s/p} > 3.5$ and $r_{s-c} < -0.6$. In contrast, models with BMO (Fig 6b) and HC (Fig 6d) LLVP compositions show more gradual changes and asymmetric "arches" skewed to the left. The BMO and HC LLVP compositions also have slightly lower peak values, with not many depths having values of $R_{s/p}$ above 2.5 and $r_{s-c}$ lower than -0.5. Additionally, for all LLVP compositions, $R_{s/p} \approx 2$ and $r_{s-c} \approx 1$ when the depth average post-perovskite fraction is 0 (depth layer contains no post-perovskite) or 1 (depth layer contains no bridgmanite). This suggests that in the absence of tomographic filtering, lowermost mantle signatures of elevated $R_{s/p}$ and $r_{s-c}$ anti-correlations cannot be explained purely by chemical heterogeneity, but can only be achieved when there is an intermediate post-perovskite fraction (i.e. a co-occurrence) of both bridgmanite and post-perovskite at the same depth.

After applying the resolving kernel to our suite of synthetic models, we obtain filtered results, where each synthetic model is averaged to one $R_{s/p}$ and one $r_{s-c}$ value (Fig. 7). All filtered models containing post-perovskite (plus sign and circle symbol) fit within $2\sigma$ uncertainty bounds of the observed $R_{s/p}$ in tomography (Fig. 7a). In particular, the models with HC LLVP composition and the model with pyrolite LLVP composition for the "partial-pPv" scenario fit within $1\sigma$ uncertainty. Conversely, all models without post-perovskite (cross sign) have $R_{s/p}$ values that are too low to fit within the $2\sigma$

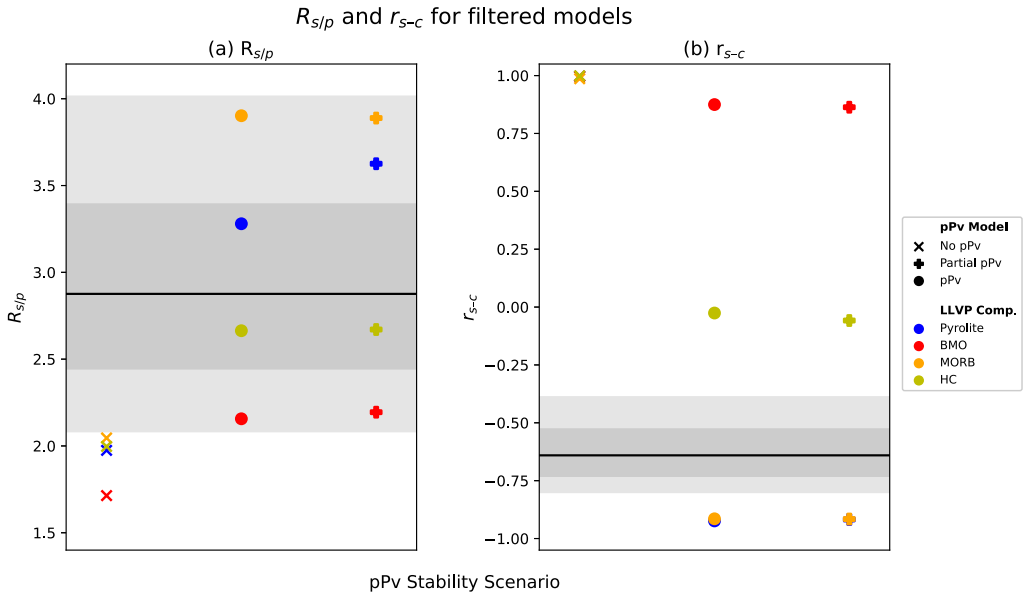


Figure 7: $R_{s/p}$ (left) and $r_{s-c}$ (right) of filtered synthetic seismic velocity models. See Fig. 5 for details of the different symbols and lines.

uncertainties of the tomographic observations. Similar patterns are observed in $r_{s-c}$ (Fig. 7b). Despite none of the synthetic seismic velocity models fitting the $2\sigma$ uncertainty of the tomographic model, those without post-perovskite only generate a positive $r_{s-c}$ and therefore cannot explain the anti-correlation that is observed in the lowermost mantle. Within the models with post-perovskite, only those with MORB and pyrolite LLVP compositions display negative $r_{s-c}$. Hence, by excluding synthetic models that do not fit within tomographic uncertainties, our results quantitatively show that models without post-perovskite do not explain both the elevated $R_{s/p}$ and negative $r_{s-c}$ signatures observed in the lowermost mantle.

## 4. Discussion

### *4.1. Co-occurrence of bridgmanite and post-perovskite*

Our study quantitatively compares synthetic seismic velocity models of various LLVP structures, compositions and post-perovskite stability scenarios with new tomography observations. We show that the ratios and correlations of velocity anomalies can only be explained when bridgmanite and post-perovskite co-occur at depth, without the need for compositional heterogeneity. Our findings are in agreement with Koelemeijer et al. (2018), who explained the elevated $R_{s/p}$ and negative $r_{s-c}$ values of SP12RTS in the lowermost mantle by the existence of both bridgmanite and post-perovskite in either a pyrolite or MORB LLVP compositions and the work of Davies et al. (2012) who showed that models containing post-perovskite better fit S40RTS than those without. Our results of $r_{s-c}$ are different from Koelemeijer et al. (2018), showing that models without post-perovskite have $r_{s-c} \approx 1$ as expected, while they found that $r_{s-c}$ can be negative at certain depths in the lowermost mantle. Koelemeijer et al. (2018) attribute this to the leakage of $V_p$ and $V_s$ structure in the joint inversion of SP12RTS. In addition, it is not guaranteed that $V_p$ and $V_s$ had the same local resolution in SP12RTS. Given we know that $V_p$ and $V_s$ resolution is nearly identical and leakage is accounted for as additional 3D noise in the tomographic model of Restelli et al. (2024), we confirm here that negative $r_{s-c}$ values in models without post-perovskite are tomographic artefacts. Our results thus confirm the presence of post-perovskite in Earth's lowermost mantle, as the tomographic uncertainties of Restelli et al. (2024) allow us to conclusively determine that models without post-perovskite do not fit with tomographic observations (Fig. 7).

Similar to Koelemeijer et al. (2018), our results additionally show that it is not the existence of post-perovskite, but a co-occurrence of both bridgmanite and post-perovskite at a given depth that explains elevated $R_{s/p}$ and negative $r_{s-c}$ in the lowermost mantle. If the elevated ratios and anti-correlation were explained purely by the presence of post-perovskite, we would expect to have the highest $R_{s/p}$ and strongest negative $r_{s-c}$ when the post-perovskite fraction is equal to 1. However, Fig. 6 shows that the strongest negative $r_{s-c}$ and highest $R_{s/p}$ for all LLVP compositions are present at intermediate post-perovskite fractions between 0.3 to 0.8, where significant fractions of both bridgmanite and post-perovskite are present.

The co-occurrence of bridgmanite and post-perovskite within the same depth happens for two reasons: (i) a bdg-pPv two-phase region in the phase diagram; or (ii) topographic variations on the bdg-pPv phase boundary in the model of the Earth. A two-phase region occurs when there is compositional variation, and one of the compositional end-member transitions to the higher-pressure phase before the other end-member. Because Fe-rich bridgmanite becomes unstable at lower pressures relative to Mg-rich bridgmanite, a mixed-phase assemblage of Fe-rich post-perovskite and Mg-rich bridgmanite can co-exist in equilibrium for pressure and temperature conditions within the two-phase region (Catalli et al., 2009; Mao et al., 2004). Topographic variations of phase transitions with non-zero Clapeyron slope exist when temperature and compositional variations at constant pressures allow both phases to co-occur at the same depth (Styles et al., 2011). A positive Clapeyron slope indicates that post-perovskite will be more stable at colder temperatures and bridgmanite at warmer temperatures at the

same pressure (Cobden et al., 2015; Hirose, 2006). We believe that a two-phase region alone is not enough to explain the increased $R_{s/p}$ and negative $r_{s-c}$ observed in seismic tomography. Even though bridgmanite and post-perovskite exist as separate phases within the two-phase region, we calculate the volume-averaged elasticity and density of the rock, so that differences in seismic velocities between the two phases are not preserved in our synthetic seismic velocity models. In contrast, lateral topography variations in a phase transition can lead to lateral differences in $V_s$ and $V_p$ relative to a 1-D average, and thus yield larger RMS velocities (Styles et al., 2011). Because the bdg-pPv phase transition increases $V_s$ by 1-4 %, the radial $V_s$ average increases when bridgmanite transitions to post-perovskite. With an increase in the radial average, the difference in $V_s$, or $d\ln V_s$, between bridgmanite and the radial average also increases (Fig. 8b). As $V_p$ does not change significantly across the phase transition, $d\ln V_p$ remains relatively constant for an increase in post-perovskite (Fig. 8a), therefore $R_{s/p}$ increases. Similarly, the decrease in $V_c$ due to the phase transition reduces the radial $V_c$ average. This increases $d\ln V_c$, but in the opposite spatial pattern to $d\ln V_s$, hence creating a negative $r_{s-c}$ (Fig. 8c). Therefore, even if a phase transition has a thick two-phase region, the topography of the phase transition is more important for seismic tomography, where velocity anomalies are typically imaged relative to a radial average (Styles et al., 2011).

### *4.2. Implications for LLVP composition*

Our study shows that composition alone is insufficient to explain the elevated $R_{s/p}$ and negative $r_{s-c}$ observed in the lowermost mantle, corroborating findings from Davies et al. (2012), Davies et al. (2015), and Koelemeijer et al.

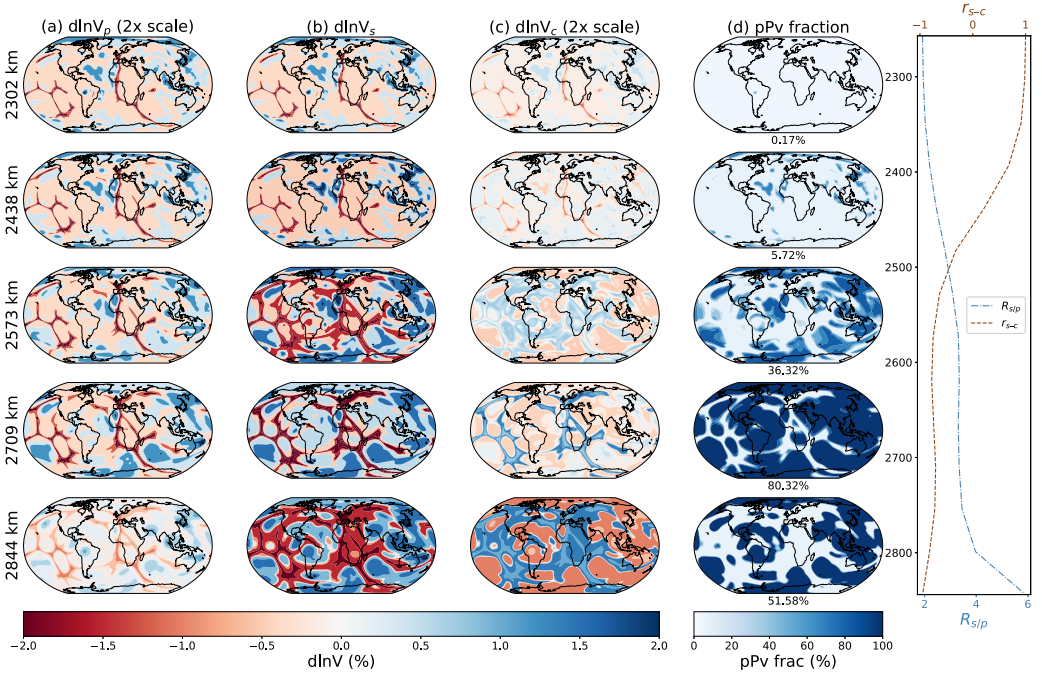


Figure 8: A series of depth slices to illustrate the effect of the co-occurrence of bridgmanite and post-perovskite (pPv) on velocity anomalies, taken from the synthetic model with the "pPv" scenario and a pyrolite composition. Depth slices in each row for $d\ln V_p$, $d\ln V_s$, $d\ln V_c$, pPv fraction from left to right. The amplitudes of $d\ln V_p$ and $d\ln V_c$ are amplified 2x relative to the seismic velocity scale bar (bottom left), so that the two plots have similar colour intensity and patterns when the $R_{s/p} = 2$. The radially averaged ratio $R_{s/p}$ (blue dashdot line) and $r_{s-c}$ (brown dashed line) with depth are shown in the rightmost plot.

(2018). Fig. 7 shows that the synthetic models of any LLVP composition without post-perovskite have $R_{s/p}$ of around 2 and $r_{s-c}$ near 1. These ratios and correlations do not fit within the tomographic observations and uncertainties of Restelli et al. (2024). Hence, we can concretely disregard the synthetic models with no post-perovskite up to a $2\sigma$ confidence level. We further examine $R_{s/p}$ separately in fast and slow clusters (defined by $d\ln V_s$ above

or below zero respectively) to study whether lateral differences in $R_{s/p}$ can yield specific information on the compositional heterogeneity of the LLVPs. However, $R_{s/p}$ values are statistically indistinguishable between the fast and slow clusters and hence do not at present provide information in addition to the results from global averages of $R_{s/p}$ (see table S3). This confirms that $R_{s/p}$ and $r_{s-c}$ are dominantly sensitive to the presence of post-perovskite in the lowermost mantle, and hence should not be used as seismic observations to argue for a compositional heterogeneous mantle (consistent with Davies et al., 2015; Koelemeijer et al., 2018; Tesoniero et al., 2016).

Our results, however, do not preclude the possibility of LLVPs as thermochemical structures. Even though ratios and correlations of seismic velocity anomalies are mostly sensitive to the bdg-pPv phase transition, other physical parameters, such as density, amplitudes of seismic velocity anomalies, and correlations between density and velocity anomalies, are used as proxies for LLVP composition (Karato and Karki, 2001; Davies et al., 2015). From our synthetic velocity models, we find that RMS velocities are relatively insensitive to the post-perovskite scenario, and instead largely reflect the combined effects of composition and temperature. Comparing synthetic RMS velocities to tomographic observations, we can quantitatively conclude that models with BMO and HC LLVP compositions do not fit the tomographic observations of both $d\ln V_s$ and $d\ln V_p$ RMS values (Fig. 5). However, none of the synthetic models yield $d\ln V_s$ RMS values that fall within the uncertainties of tomographic observations. A possible explanation is the oversimplification of our assumed LLVP compositions, i.e. the fact that we assume one constant composition for the entire LLVP (based on the compositional field of the geo-

dynamic model of Davies et al. (2012)). However, LLVPs could be composed of a mixture or layers of different compositions (Ballmer et al., 2016; Jones et al., 2021; Tackley, 2012). For example, Richards et al. (2023) recently suggested that LLVPs are mostly thermal features that only contain denser compositionally distinct material in the lowest part. We examine this idea in an additional set of synthetic seismic velocity models where the LLVPs only contain compositionally distinct material in the bottom 200 km of the mantle. These models have more comparable amplitudes to the tomography model, such that models of pyrolite and MORB LLVP composition fit within the uncertainties of both $d \ln V_p$ and $d \ln V_s$ RMS values (Fig. S5). However, this is not consistent with the geodynamic model simulations and it is therefore important that models with layered LLVPs are explored further in geodynamic studies to assess this idea properly.

Additionally, we cannot attribute the misfit of our synthetic seismic velocity models entirely to oversimplification in LLVP composition alone. This is because all of our models also fall outside tomographic uncertainties of $r_{s-c}$ (Fig. 7), which we show is predominantly a proxy for the co-occurrence of both bridgmanite and post-perovskite. Therefore, the assumptions of the dynamic effects and thermodynamic properties of post-perovskite in our synthetic models can also contribute to the misfit. Post-perovskite is thought to destabilise the thermal boundary layer above the CMB and promote plume formation, thus influencing lower mantle thermochemical structures (Ammann et al., 2014; Hunt et al., 2012; Nakagawa and Tackley, 2004). These dynamic effects should ideally be included, but a quantification of these effects will be prone to uncertainty, especially when considering anisotropy and

possible slip mechanisms of post-perovskite (Cobden et al., 2015; Goryaeva et al., 2016). Furthermore, these effects are unlikely to be visible in our results, given that we only consider depth averages of laterally averaged, long-wavelength, present-day tomographic signatures in a broad depth interval of the lowermost mantle.

Approximations in the equations of state, as well as uncertainties in experimental pressure scales lead to large uncertainties in the thermodynamic parameters at lowermost mantle conditions. Consequently, the dependence of the synthetic elastic parameters on the assumed mineral physics model can also contribute to the misfit of $d\ln V_s$ RMS and $r_{s-c}$ between the synthetic models and tomographic observations. For example, we have noted that for models with a pyrolite or MORB LLVP composition, the exclusion or addition of post-perovskite leads to too low or too high $d\ln V_s$ RMS values (Fig. 5), while $r_{s-c}$ shifts from strongly positive to strongly negative when post-perovskite is added. Given the large uncertainties in the thermodynamic parameters of post-perovskite (Cobden et al., 2015), it is therefore possible that changes in these parameters, especially the shear modulus, could give results that fit both $d\ln V_s$ RMS and $r_{s-c}$ values within tomographic uncertainties. We conduct additional comparisons with synthetic models calculated using the mineralogical model SLB2011 (Stixrude and Lithgow-Bertelloni, 2011) to test the sensitivity of our results to the assumed mineral physics parameters. Despite significant differences in the bdg-pPv phase boundary (Fig. S3), we obtain similar results that support our overall findings: Fe-rich compositions show RMS velocity anomalies that are too large to explain tomographic observations (Fig. S2), and a co-occurrence of bridgmanite and post-perovskite

is required to explain values of elevated $R_{s/p}$ and negative $r_{s-c}$ in the lowermost mantle (Fig. S4). The dependence of our results on assumptions in the mineral physics parameters could be better quantified if both errors and covariances on the various thermodynamic parameters were available. Hence, future tomographic-geodynamic comparison studies will benefit from a full quantification of mineral physics uncertainties that can be propagated into elastic parameters.

### *4.3. Towards a better understanding of the bdg-ppv phase transition*

Given that elevated $R_{s/p}$ ratios and $r_{s-c}$ anti-correlations are both indicators of the co-occurrence of bridgmanite and post-perovskite, we expect these signatures to get stronger at depths where the pPv fraction is between 20-80 %. This raises the possibility to use these signatures to constrain the two-phase region and depth of the bdg-pPv phase transition. However, in this instance, we cannot constrain this depth as the tomographic model of Restelli et al. (2024) only offers a depth-averaged image of the lowermost mantle. Although the thickness of the two-phase region may affect the strength of $R_{s/p}$ and $r_{s-c}$ after tomographic filtering, we cannot interpret the model amplitudes in this way, given the tomographic uncertainties of Restelli et al. (2024). Similarly, we cannot determine whether a double-crossing of post-perovskite at the base of the mantle occurs, as suggested by previous studies (Hernlund et al., 2005). In our unfiltered results, we see that post-perovskite transitions back to bridgmanite at the base of the mantle due to a steep increase in temperature (Fig. 6). However, this is heavily dependent on the choice of the mineralogical model, as the double-crossing is not observed in synthetic tomographic images calculated with the SLB2011 mineralogical

model (Koelemeijer et al., 2018). Future improvements in seismic tomography to obtain better depth resolution with uncertainties will make it possible to better constrain the thickness and depth of the bdg-pPv phase boundary and the existence of the double-crossing.

Given that experimental studies have shown that post-perovskite can be highly anisotropic under lowermost mantle conditions (Iitaka et al., 2004; Tsuchiya et al., 2004), seismic anisotropy may be a useful tool to determine the distribution of post-perovskite in the lowermost mantle (Asplet et al., 2022; Nowacki et al., 2011). However, including seismic anisotropy in tomographic-geodynamic model comparisons is challenging at present. First, the dominant slip plane of post-perovskite at lowermost mantle conditions remains debated, but strongly influences the seismic anisotropy signatures (Cottaar et al., 2014; Ward et al., 2024). Second, Ward et al. (2024) demonstrate that calculations of seismic anisotropy based on geodynamic modelling requires a full history of the flow field, which is not available for the suite of geodynamic models used in this study. Third, global tomography models of seismic anisotropy are highly variable due to imbalances between $V_{sh}$ and $V_{sv}$ sensitive data used to sample the lowermost mantle, and further impacted by the assumed crustal corrections (Chang and Ferreira, 2017; Kustowski et al., 2008; Restelli et al., 2022). Therefore, further efforts are required to improve seismic anisotropy tomography and synthetic calculations of post-perovskite anisotropy, before we can use seismic anisotropy as a tool to constrain the post-perovskite distribution in the lowermost mantle.

## 5. Conclusion

We quantitatively investigate the nature of the LLVPs by comparing a Backus-Gilbert (BG) tomographic model with synthetic seismic velocity models for various LLVP compositions and post-perovskite stability scenarios. The BG model provides robust ratios and correlations of seismic velocity variations derived from nearly equal $V_p$ and $V_s$ resolution, and includes uncertainty quantification that encompasses both data and theoretical errors. By rejecting synthetic models that do not fit within tomographic uncertainties, we show that two groups of models cannot explain lowermost mantle tomographic signatures. First, iron-rich compositions result in velocity anomaly amplitudes that are too large to explain tomographic observations. Second, models without the post-perovskite phase fail to generate the elevated $R_{s/p}$ ratio ($d\ln V_s/d\ln V_p$) and $r_{s\text{–}c}$ ($d\ln V_s$-$d\ln V_c$) anti-correlation observed in the lowermost mantle, while these can be explained by a co-occurrence of bridgmanite and post-perovskite. Our results thus show that the effects of lowermost mantle composition and mineralogy can be separated, with the effects of temperature and composition primarily captured in the amplitudes of seismic velocity anomalies, and those of phase transition represented by the ratios and correlations. This confirms that $R_{s/p}$ and $r_{s\text{–}c}$ should not be used as arguments for chemical heterogeneity in the lowermost mantle. However, neither do our results imply that LLVPs are purely thermal features, and we instead encourage further research using other seismic and geodetic observations to better constrain the composition and origin of LLVPs.

## CRediT authorship contribution statement

**Justin Leung:** Conceptualization, Data curation, Funding acquisition, Methodology, Software, Visualization, Writing – original draft, Writing – review & editing. **Andrew M. Walker:** Conceptualization, Methodology, Project administration, Software, Supervision, Writing – review & editing. **Paula Koelemeijer:** Conceptualization, Funding acquisition, Methodology, Software, Supervision, Writing – review & editing. **Federica Restelli:** Data Curation, Writing – review & editing. **D. Rhodri Davies:** Data Curation, Writing – review & editing.

## Acknowledgments

The authors would like to thank the guest editors Lauren Waszek, Mathieu Dumberry, and Mike Bergman for putting together the SEDI special issue, as well as two anonymous reviewers for their constructive comments. J.L. received funding from a NERC DTP Award (NE/S007474/1). J.L. also acknowledges the financial support from SEDI to attend the 18th SEDI Symposium in Great Barrington (2024). P.K. acknowledges financial support from a Royal Society University Research Fellowship (URF\R1\180377). For the purpose of Open Access, the authors have applied a CC BY public copyright licence to any Author Accepted Manuscript (AAM) version arising from this submission.

## Data Availability

The Python used for the analysis and figure production in this manuscript can be found online at https://doi.org/10.5281/zenodo.15810581. For access

to the data used in this study, please contact D.R.D. (rhodri.davies@anu.edu.au) for the geodynamic input fields and P.K. (paula.koelemeijer@earth.ox.ac.uk) for the seismic tomography model.

## References


Akbarashrafi, F., Al-Attar, D., Deuss, A., Trampert, J., Valentine, A.P., 2018. Exact free oscillation spectra, splitting functions and the resolvability of Earth's density structure. Geophysical Journal International 213, 58–76. URL: https://academic.oup.com/gji/article/213/1/58/4757069, doi:10.1093/gji/ggx539.

Ammann, M.W., Brodholt, J.P., Wookey, J., Dobson, D.P., 2010. First-principles constraints on diffusion in lower-mantle minerals and a weak D layer. Nature 465, 462–465. URL: https://www.nature.com/articles/nature09052, doi:10.1038/nature09052.

Ammann, M.W., Walker, A.M., Stackhouse, S., Wookey, J., Forte, A.M., Brodholt, J.P., Dobson, D.P., 2014. Variation of thermal conductivity and heat flux at the Earth's core mantle boundary. Earth and Planetary Science Letters 390, 175–185. URL: https://linkinghub.elsevier.com/retrieve/pii/S0012821X14000120, doi:10.1016/j.epsl.2014.01.009.

Asplet, J., Wookey, J., Kendall, M., 2022. Inversion of shear wave waveforms reveal deformation in the lowermost mantle. Geophysical Journal International 232, 97–114. URL:

https://academic.oup.com/gji/article/232/1/97/6677397, doi:10.1093/gji/ggac328.

Ballmer, M.D., Schumacher, L., Lekic, V., Thomas, C., Ito, G., 2016. Compositional layering within the large low shear-wave velocity provinces in the lower mantle. Geochem. Geophys. Geosyst. 17, 5056–5077. URL: https://onlinelibrary.wiley.com/doi/10.1002/2016GC006605, doi:10.1002/2016GC006605.

Bull, A., McNamara, A., Ritsema, J., 2009. Synthetic tomography of plume clusters and thermochemical piles. Earth and Planetary Science Letters 278, 152–162. URL: https://linkinghub.elsevier.com/retrieve/pii/S0012821X08007309, doi:10.1016/j.epsl.2008.11.018.

Burke, K., Steinberger, B., Torsvik, T.H., Smethurst, M.A., 2008. Plume Generation Zones at the margins of Large Low Shear Velocity Provinces on the core–mantle boundary. Earth and Planetary Science Letters 265, 49–60. URL: https://linkinghub.elsevier.com/retrieve/pii/S0012821X07006036, doi:10.1016/j.epsl.2007.09.042.

Catalli, K., Shim, S.H., Prakapenka, V., 2009. Thickness and Clapeyron slope of the post-perovskite boundary. Nature 462, 782–785. URL: https://www.nature.com/articles/nature08598, doi:10.1038/nature08598.

Chang, S., Ferreira, A.M.G., 2017. Improving Global Ra-

dial Anisotropy Tomography: The Importance of Simultaneously Inverting for Crustal and Mantle Structure. Bulletin of the Seismological Society of America 107, 624–638. URL: https://pubs.geoscienceworld.org/bssa/article/107/2/624-638/354155, doi:10.1785/0120160142.

Cobden, L., Thomas, C., Trampert, J., 2015. Seismic Detection of Post-perovskite Inside the Earth, in: Khan, A., Deschamps, F. (Eds.), The Earth's Heterogeneous Mantle. Springer International Publishing, Cham, pp. 391–440. doi:10.1007/978-3-319-15627-9_13.

Cottaar, S., Lekic, V., 2016. Morphology of seismically slow lower-mantle structures. Geophysical Journal International 207, 1122–1136. URL: https://academic.oup.com/gji/article/207/2/1122/2583772, doi:10.1093/gji/ggw324.

Cottaar, S., Li, M., McNamara, A.K., Romanowicz, B., Wenk, H.R., 2014. Synthetic seismic anisotropy models within a slab impinging on the core–mantle boundary. Geophysical Journal International 199, 164–177. URL: http://academic.oup.com/gji/article/199/1/164/725490/Synthetic-seismic-anisotrop doi:10.1093/gji/ggu244.

Davies, D., Goes, S., Lau, H., 2015. Thermally dominated deep mantle llsvps: a review. The Earth's Heterogeneous Mantle: A Geophysical, Geodynamical, and Geochemical Perspective , 441–477.

Davies, D.R., Davies, J.H., Bollada, P.C., Hassan, O., Morgan, K.,

Nithiarasu, P., 2013. A hierarchical mesh refinement technique for global 3-d spherical mantle convection modelling. Geoscientific Model Development 6, 1095–1107.

Davies, D.R., Ghelichkhan, S., Hoggard, M., Valentine, A.P., Richards, F.D., 2023. Observations and models of dynamic topography: Current status and future directions. Dynamics of plate tectonics and mantle convection , 223–269.

Davies, D.R., Goes, S., Davies, J., Schuberth, B., Bunge, H.P., Ritsema, J., 2012. Reconciling dynamic and seismic models of Earth's lower mantle: The dominant role of thermal heterogeneity. Earth and Planetary Science Letters 353-354, 253–269. URL: https://linkinghub.elsevier.com/retrieve/pii/S0012821X1200444X, doi:10.1016/j.epsl.2012.08.016.

Dziewonski, A.M., Anderson, D.L., 1981. Preliminary reference Earth model. Physics of the Earth and Planetary Interiors 25, 297–356. URL: https://www.sciencedirect.com/science/article/pii/0031920181900467, doi:https://doi.org/10.1016/0031-9201(81)90046-7.

Edmonds, A., 1960. Angular Momentum in Quantum Mechanics. Number 4 in Investigations in physics, Princeton University Press.

Forte, A.M., Simmons, N.A., Grand, S.P., 2015. 1.27 - Constraints on Seismic Models from Other Disciplines - Constraints on 3-D Seismic Models from Global Geodynamic Observables: Implications for the Global Mantle Convective Flow, in: Schubert, G. (Ed.), Treatise on Geophysics

(Second Edition). second edition ed.. Elsevier, Oxford, pp. 853–907. URL: https://www.sciencedirect.com/science/article/pii/B9780444538024000282, doi:https://doi.org/10.1016/B978-0-444-53802-4.00028-2.

Garnero, E.J., McNamara, A.K., Shim, S.H., 2016. Continent-sized anomalous zones with low seismic velocity at the base of Earth's mantle. Nature Geosci 9, 481–489. URL: https://www.nature.com/articles/ngeo2733, doi:10.1038/ngeo2733.

Goryaeva, A.M., Carrez, P., Cordier, P., 2016. Low viscosity and high attenuation in MgSiO3 post-perovskite inferred from atomic-scale calculations. Sci Rep 6, 34771. URL: https://www.nature.com/articles/srep34771, doi:10.1038/srep34771.

Hager, B.H., Clayton, R.W., Richards, M.A., Comer, R.P., Dziewonski, A.M., 1985. Lower mantle heterogeneity, dynamic topography and the geoid. Nature 313, 541–545. URL: https://www.nature.com/articles/313541a0, doi:10.1038/313541a0.

Hernlund, J.W., Thomas, C., Tackley, P.J., 2005. A doubling of the post-perovskite phase boundary and structure of the Earth's lowermost mantle. Nature 434, 882–886. URL: https://www.nature.com/articles/nature03472, doi:10.1038/nature03472.

Hirose, K., 2006. Postperovskite phase transition and its geophysical implications. Rev. Geophys. 44, RG3001.

URL: http://doi.wiley.com/10.1029/2005RG000186, doi:10.1029/2005RG000186.

Hirose, K., Takafuji, N., Sata, N., Ohishi, Y., 2005. Phase transition and density of subducted MORB crust in the lower mantle. Earth and Planetary Science Letters 237, 239–251. URL: https://linkinghub.elsevier.com/retrieve/pii/S0012821X0500419X, doi:10.1016/j.epsl.2005.06.035.

Hunt, S.A., Davies, D.R., Walker, A.M., McCormack, R.J., Wills, A.S., Dobson, D.P., Li, L., 2012. On the increase in thermal diffusivity caused by the perovskite to post-perovskite phase transition and its implications for mantle dynamics. Earth and Planetary Science Letters 319-320, 96–103. URL: https://linkinghub.elsevier.com/retrieve/pii/S0012821X11007230, doi:10.1016/j.epsl.2011.12.009.

Iitaka, T., Hirose, K., Kawamura, K., Murakami, M., 2004. The elasticity of the MgSiO3 post-perovskite phase in the Earth's lowermost mantle. Nature 430, 442–445. URL: https://www.nature.com/articles/nature02702, doi:10.1038/nature02702.

Irifune, T., Tsuchiya, T., 2015. 2.03 - Phase Transitions and Mineralogy of the Lower Mantle, in: Schubert, G. (Ed.), Treatise on Geophysics (Second Edition). second edition ed.. Elsevier, Oxford, pp. 33–60. URL: https://www.sciencedirect.com/science/article/pii/B9780444538024000300, doi:https://doi.org/10.1016/B978-0-444-53802-4.00030-0.

Ishii, M., Tromp, J., 1999. Normal-Mode and Free-Air Grav-

807 ity Constraints on Lateral Variations in Velocity and Den-
808 sity of Earth's Mantle. Science 285, 1231–1236. URL:
809 https://www.science.org/doi/10.1126/science.285.5431.1231,
810 doi:10.1126/science.285.5431.1231.

811 Jones, T., Sime, N., Van Keken, P., 2021. Burying earth's primitive man-
812 tle in the slab graveyard. Geochemistry, Geophysics, Geosystems 22,
813 e2020GC009396.

814 Jones, T.D., Maguire, R.R., Van Keken, P.E., Ritsema, J., Koelemei-
815 jer, P., 2020. Subducted oceanic crust as the origin of seismically
816 slow lower-mantle structures. Prog Earth Planet Sci 7, 17. URL:
817 https://progearthplanetsci.springeropen.com/articles/10.1186/s40645-020-00327-1,
818 doi:10.1186/s40645-020-00327-1.

819 Karato, S., Karki, B.B., 2001. Origin of lateral variation of seis-
820 mic wave velocities and density in the deep mantle. Journal
821 of Geophysical Research: Solid Earth 106, 21771–21783. URL:
822 https://agupubs.onlinelibrary.wiley.com/doi/10.1029/2001JB000214,
823 doi:10.1029/2001JB000214.

824 Koelemeijer, P., Deuss, A., Ritsema, J., 2017. Density structure of Earth's
825 lowermost mantle from Stoneley mode splitting observations. Nat Com-
826 mun 8, 15241. URL: https://www.nature.com/articles/ncomms15241,
827 doi:10.1038/ncomms15241.

828 Koelemeijer, P., Ritsema, J., Deuss, A., Van Heijst, H.J., 2016.
829 SP12RTS: a degree-12 model of shear- and compressional-wave ve-

locity for Earth's mantle. Geophys. J. Int. 204, 1024–1039. URL: https://academic.oup.com/gji/article-lookup/doi/10.1093/gji/ggv481, doi:10.1093/gji/ggv481.

Koelemeijer, P., Schuberth, B., Davies, D., Deuss, A., Ritsema, J., 2018. Constraints on the presence of post-perovskite in Earth's lowermost mantle from tomographic-geodynamic model comparisons. Earth and Planetary Science Letters 494, 226–238. URL: https://linkinghub.elsevier.com/retrieve/pii/S0012821X18302656, doi:10.1016/j.epsl.2018.04.056.

Kustowski, B., Ekström, G., Dziewoński, A.M., 2008. Anisotropic shear-wave velocity structure of the Earth's mantle: A global model. J. Geophys. Res. 113, 2007JB005169. URL: https://agupubs.onlinelibrary.wiley.com/doi/10.1029/2007JB005169, doi:10.1029/2007JB005169.

Labrosse, S., Hernlund, J.W., Coltice, N., 2007. A crystallizing dense magma ocean at the base of the Earth's mantle. Nature 450, 866–869. URL: https://www.nature.com/articles/nature06355, doi:10.1038/nature06355.

Lau, H.C.P., Mitrovica, J.X., Davis, J.L., Tromp, J., Yang, H.Y., Al-Attar, D., 2017. Tidal tomography constrains Earth's deep-mantle buoyancy. Nature 551, 321–326. URL: https://www.nature.com/articles/nature24452, doi:10.1038/nature24452.

853 Lee, C.T.A., Luffi, P., Höink, T., Li, J., Dasgupta, R., Hern-
854 lund, J., 2010. Upside-down differentiation and genera-
855 tion of a 'primordial' lower mantle. Nature 463, 930–
856 933. URL: https://www.nature.com/articles/nature08824,
857 doi:10.1038/nature08824.

858 Mao, W.L., Shen, G., Prakapenka, V.B., Meng, Y., Camp-
859 bell, A.J., Heinz, D.L., Shu, J., Hemley, R.J., Mao, H.k.,
860 2004. Ferromagnesian postperovskite silicates in the D layer
861 of the Earth. Proc. Natl. Acad. Sci. U.S.A. 101, 15867–15869.
862 URL: https://pnas.org/doi/full/10.1073/pnas.0407135101,
863 doi:10.1073/pnas.0407135101.

864 Masters, G., Gubbins, D., 2003. On the resolution of density within the
865 Earth. Physics of the Earth and Planetary Interiors 140, 159–167. URL:
866 https://linkinghub.elsevier.com/retrieve/pii/S0031920103001705,
867 doi:10.1016/j.pepi.2003.07.008.

868 Masters, G., Laske, G., Bolton, H., Dziewonski, A., 2000. The Relative
869 Behavior of Shear Velocity, Bulk Sound Speed, and Compressional Velocity
870 in the Mantle: Implications for Chemical and Thermal Structure. Earth's
871 Deep Interior: Mineral Physics and Tomography From the Atomic to the
872 Global Scale 117, 63–87. doi:10.1029/GM117p0063. place: Washington, D.
873 C Publisher: American Geophysical Union.

874 McNamara, A.K., 2019. A review of large low shear velocity provinces
875 and ultra low velocity zones. Tectonophysics 760, 199–220. URL:

876 https://linkinghub.elsevier.com/retrieve/pii/S0040195118301586,
877 doi:10.1016/j.tecto.2018.04.015.

878 Moulik, P., Ekström, G., 2016. The relationships between large-scale
879 variations in shear velocity, density, and compressional velocity
880 in the Earth's mantle. JGR Solid Earth 121, 2737–2771. URL:
881 https://agupubs.onlinelibrary.wiley.com/doi/10.1002/2015JB012679,
882 doi:10.1002/2015JB012679.

883 Murakami, M., Hirose, K., Kawamura, K., Sata, N., Ohishi, Y., 2004.
884 Post-Perovskite Phase Transition in MgSiO $_3$. Science 304, 855–
885 858. URL: https://www.science.org/doi/10.1126/science.1095932,
886 doi:10.1126/science.1095932.

887 Myhill, R., Cottaar, S., Heister, T., Rose, I., Unterborn, C., Dannberg,
888 J., Gassmoeller, R., 2023. BurnMan – a Python toolkit for
889 planetary geophysics,geochemistry and thermodynamics. JOSS 8,
890 5389. URL: https://joss.theoj.org/papers/10.21105/joss.05389,
891 doi:10.21105/joss.05389.

892 Nakagawa, T., Tackley, P.J., 2004. Effects of a perovskite-post per-
893 ovskite phase change near core-mantle boundary in compressible mantle
894 convection. Geophysical Research Letters 31, 2004GL020648. URL:
895 https://agupubs.onlinelibrary.wiley.com/doi/10.1029/2004GL020648,
896 doi:10.1029/2004GL020648.

897 Ni, S., Tan, E., Gurnis, M., Helmberger, D., 2002. Sharp
898 Sides to the African Superplume. Science 296, 1850–1852.

URL: https://www.science.org/doi/10.1126/science.1070698, doi:10.1126/science.1070698.

Niu, Y., 2018. Origin of the LLSVPs at the base of the mantle is a consequence of plate tectonics – A petrological and geochemical perspective. Geoscience Frontiers 9, 1265–1278. URL: https://linkinghub.elsevier.com/retrieve/pii/S1674987118300847, doi:10.1016/j.gsf.2018.03.005.

Nowacki, A., Wookey, J., Kendall, J.M., 2011. New advances in using seismic anisotropy, mineral physics and geodynamics to understand deformation in the lowermost mantle. Journal of Geodynamics 52, 205–228. URL: https://linkinghub.elsevier.com/retrieve/pii/S0264370711000573, doi:10.1016/j.jog.2011.04.003.

Oganov, A.R., Ono, S., 2004. Theoretical and experimental evidence for a post-perovskite phase of MgSiO3 in Earth's D layer. Nature 430, 445–448. URL: https://doi.org/10.1038/nature02701, doi:10.1038/nature02701.

Panton, J., Davies, J.H., Koelemeijer, P., Myhill, R., Ritsema, J., 2025. Unique composition and evolutionary histories of large low velocity provinces. Scientific Reports 15, 4466. URL: https://www.nature.com/articles/s41598-025-88931-3, doi:10.1038/s41598-025-88931-3.

Restelli, F., Koelemeijer, P., Ferreira, A.M.G., 2022. Normal mode observability of radial anisotropy in the Earth's man-

922 tle. Geophysical Journal International 233, 663–679. URL:
923 https://academic.oup.com/gji/article/233/1/663/6862098,
924 doi:10.1093/gji/ggac474.

925 Restelli, F., Zaroli, C., Koelemeijer, P., 2024. Robust estimates of the ratio
926 between S- and P-wave velocity anomalies in the Earth's mantle using nor-
927 mal modes. Physics of the Earth and Planetary Interiors 347, 107135. URL:
928 https://linkinghub.elsevier.com/retrieve/pii/S0031920123001619,
929 doi:10.1016/j.pepi.2023.107135.

930 Richards, F.D., Hoggard, M.J., Ghelichkhan, S., Koelemei-
931 jer, P., Lau, H.C., 2023. Geodynamic, geodetic, and seis-
932 mic constraints favour deflated and dense-cored LLVPs.
933 Earth and Planetary Science Letters 602, 117964. URL:
934 https://linkinghub.elsevier.com/retrieve/pii/S0012821X22006008,
935 doi:10.1016/j.epsl.2022.117964.

936 Ritsema, J., Deuss, A., Van Heijst, H.J., Woodhouse, J.H.,
937 2011. S40RTS: a degree-40 shear-velocity model for the man-
938 tle from new Rayleigh wave dispersion, teleseismic traveltime
939 and normal-mode splitting function measurements: S40RTS.
940 Geophysical Journal International 184, 1223–1236. URL:
941 https://academic.oup.com/gji/article-lookup/doi/10.1111/j.1365-246X.2010.04884.x
942 doi:10.1111/j.1365-246X.2010.04884.x.

943 Ritsema, J., Van Heijst, H.J., 2002. Constraints on the correlation of $P$ -
944 and $S$ -wave velocity heterogeneity in the mantle from $P$ , $PP$ , $PPP$ and
945 $PKP$ ab traveltimes. Geophysical Journal International 149, 482–489.

URL: https://academic.oup.com/gji/article/149/2/482/728317, doi:10.1046/j.1365-246X.2002.01631.x.

Robson, A., Lau, H.C.P., Koelemeijer, P., Romanowicz, B., 2021. An analysis of core–mantle boundary Stoneley mode sensitivity and sources of uncertainty. Geophysical Journal International 228, 1962–1974. URL: https://academic.oup.com/gji/article/228/3/1962/6413994, doi:10.1093/gji/ggab448.

Schubert, G., Masters, G., Olson, P., Tackley, P., 2004. Superplumes or plume clusters? Physics of the Earth and Planetary Interiors 146, 147–162. URL: https://linkinghub.elsevier.com/retrieve/pii/S0031920104001128, doi:10.1016/j.pepi.2003.09.025.

Schuberth, B.S.A., Bunge, H., Ritsema, J., 2009a. Tomographic filtering of high-resolution mantle circulation models: Can seismic heterogeneity be explained by temperature alone? Geochem Geophys Geosyst 10, 2009GC002401. URL: https://agupubs.onlinelibrary.wiley.com/doi/10.1029/2009GC002401, doi:10.1029/2009GC002401.

Schuberth, B.S.A., Bunge, H., Steinle-Neumann, G., Moder, C., Oeser, J., 2009b. Thermal versus elastic heterogeneity in high-resolution mantle circulation models with pyrolite composition: High plume excess temperatures in the lowermost mantle. Geochem Geophys Geosyst 10, 2008GC002235. URL:

https://agupubs.onlinelibrary.wiley.com/doi/10.1029/2008GC002235, doi:10.1029/2008GC002235.

Stampfli, G., Borel, G., 2002. A plate tectonic model for the Paleozoic and Mesozoic constrained by dynamic plate boundaries and restored synthetic oceanic isochrons. Earth and Planetary Science Letters 196, 17–33. URL: https://linkinghub.elsevier.com/retrieve/pii/S0012821X0100588X, doi:10.1016/S0012-821X(01)00588-X.

Stampfli, G.M., Hochard, C., 2009. Plate tectonics of the Alpine realm. SP 327, 89–111. URL: https://www.lyellcollection.org/doi/10.1144/SP327.6, doi:10.1144/SP327.6.

Stixrude, L., Lithgow-Bertelloni, C., 2011. Thermodynamics of mantle minerals - II. Phase equilibria. Geophysical Journal International 184, 1180–1213. URL: https://academic.oup.com/gji/article/184/3/1180/625783, doi:10.1111/j.1365-246X.2010.04890.x.

Stixrude, L., Lithgow-Bertelloni, C., 2021. Thermal expansivity, heat capacity and bulk modulus of the mantle. Geophysical Journal International 228, 1119–1149. URL: https://academic.oup.com/gji/article/228/2/1119/6375416, doi:10.1093/gji/ggab394.

Styles, E., Davies, D.R., Goes, S., 2011. Mapping spherical seismic into physical structure: biases from 3-D phase-transition and ther-

mal boundary-layer heterogeneity: 3-D biases in 1-D seismic velocities. Geophysical Journal International 184, 1371–1378. URL: https://academic.oup.com/gji/article-lookup/doi/10.1111/j.1365-246X.2010.04914.x doi:10.1111/j.1365-246X.2010.04914.x.

Su, J., Houser, C., Hernlund, J.W., Deschamps, F., 2023. Tomographic filtering of shear and compressional wave models reveals uncorrelated variations in the lowermost mantle. Geophysical Journal International 234, 2114–2127. URL: https://academic.oup.com/gji/article/234/3/2114/7172860, doi:10.1093/gji/ggad190.

Su, W.j., Dziewonski, A.M., 1997. Simultaneous inversion for 3-D variations in shear and bulk velocity in the mantle. Physics of the Earth and Planetary Interiors 100, 135–156. URL: https://linkinghub.elsevier.com/retrieve/pii/S0031920196032360, doi:10.1016/S0031-9201(96)03236-0.

Tackley, P.J., 2012. Dynamics and evolution of the deep mantle resulting from thermal, chemical, phase and melting effects. Earth-Science Reviews 110, 1–25. URL: https://linkinghub.elsevier.com/retrieve/pii/S0012825211001486, doi:10.1016/j.earscirev.2011.10.001.

Tarduno, J.A., Watkeys, M.K., Huffman, T.N., Cottrell, R.D., Blackman, E.G., Wendt, A., Scribner, C.A., Wagner, C.L., 2015. Antiquity of the South Atlantic Anomaly and evidence for top-down control on the geodynamo. Nat Commun 6,

7865. URL: https://www.nature.com/articles/ncomms8865, doi:10.1038/ncomms8865.

Tesoniero, A., Cammarano, F., Boschi, L., 2016. StoP heterogeneity ratio in the lower mantle and thermo-chemical implications. Geochem Geophys Geosyst 17, 2522–2538. URL: https://agupubs.onlinelibrary.wiley.com/doi/10.1002/2016GC006293, doi:10.1002/2016GC006293.

Thorne, M.S., Garnero, E.J., Grand, S.P., 2004. Geographic correlation between hot spots and deep mantle lateral shear-wave velocity gradients. Physics of the Earth and Planetary Interiors 146, 47–63. URL: https://linkinghub.elsevier.com/retrieve/pii/S003192010400113X, doi:10.1016/j.pepi.2003.09.026.

Tolstikhin, I., Hofmann, A.W., 2005. Early crust on top of the Earth's core. Physics of the Earth and Planetary Interiors 148, 109–130. URL: https://linkinghub.elsevier.com/retrieve/pii/S0031920104002961, doi:10.1016/j.pepi.2004.05.011.

Trampert, J., Deschamps, F., Resovsky, J., Yuen, D., 2004. Probabilistic Tomography Maps Chemical Heterogeneities Throughout the Lower Mantle. Science 306, 853–856. URL: https://www.science.org/doi/10.1126/science.1101996, doi:10.1126/science.1101996.

Trautner, V.E., Stackhouse, S., Turner, A.R., Koelemeijer, P., Davies, D.R., Méndez, A.S.J., Satta, N., Kurnosov, A., Liermann, H.P.,

Marquardt, H., 2023. Compressibility of ferropericlase at high-temperature: Evidence for the iron spin crossover in seismic tomography. Earth and Planetary Science Letters 618, 118296. URL: https://linkinghub.elsevier.com/retrieve/pii/S0012821X23003096, doi:10.1016/j.epsl.2023.118296.

Tsuchiya, T., Tsuchiya, J., Umemoto, K., Wentzcovitch, R.M., 2004. Elasticity of post-perovskite $MgSiO_3$. Geophysical Research Letters 31, 2004GL020278. URL: https://agupubs.onlinelibrary.wiley.com/doi/10.1029/2004GL020278, doi:10.1029/2004GL020278.

Ward, J., Nowacki, A., Rost, S., 2020. Lateral Velocity Gradients in the African Lower Mantle Inferred From Slowness Space Observations of Multipathing. Geochem Geophys Geosyst 21, e2020GC009025. URL: https://agupubs.onlinelibrary.wiley.com/doi/10.1029/2020GC009025, doi:10.1029/2020GC009025.

Ward, J., Walker, A.M., Nowacki, A., Panton, J., Davies, J.H., 2024. The sensitivity of lowermost mantle anisotropy to past mantle convection. Physics of the Earth and Planetary Interiors 356, 107264. URL: https://linkinghub.elsevier.com/retrieve/pii/S0031920124001225, doi:10.1016/j.pepi.2024.107264.

Zaroli, C., 2016. Global seismic tomography using Backus–Gilbert inversion. Geophys. J. Int. 207, 876–888. URL: https://academic.oup.com/gji/article-lookup/doi/10.1093/gji/ggw315, doi:10.1093/gji/ggw315.